npg

ORIGINAL ARTICLE

Kinetic modeling of the monoamine oxidase B radioligand [^{11}C]SL25.1188 in human brain with high-resolution positron emission tomography

Pablo M Rusjan[1], Alan A Wilson[1,2], Laura Miler[1], Ian Fan[1], Romina Mizrahi[1,2], Sylvain Houle[1,2], Neil Vasdev[3] and Jeffrey H Meyer[1,2]

This article describes the kinetic modeling of [^{11}C]SL25.1188 ([(S)-5-methoxymethyl-3-[6-(4,4,4-trifluorobutoxy)-benzo[d]isoxazol-3-yl]-oxazolidin-2-[^{11}C]one]) binding to monoamine oxidase B (MAO-B) in the human brain using high-resolution positron emission tomography (PET). Seven healthy subjects underwent two separate 90- minute PET scans after an intravenous injection of [^{11}C]SL25.1188. Complementary arterial blood sampling was acquired. Radioactivity was quickly eliminated from plasma with 80% of parent compound remaining at 90 minutes. Metabolites were more polar than the parent compound. Time-activity curves showed high brain uptake, early peak and washout rate consistent with known regional MAO-B concentration. A two-tissue compartment model (2-TCM) provided better fits to the data than a 1-TCM. Measurement of total distribution volume (V_T) showed very good identifiability (based on coefficient of variation (COV)) for all regions of interest (ROIs) (COV(V_T) < 8%), low between-subject variability ($\sim$20%), and quick temporal convergence (within 5% of final value at 45 minutes). Logan graphical method produces very good estimation of V_T. Regional V_T highly correlated with previous postmortem report of MAO-B level ($r^2 = \geqslant 0.9$). Specific binding would account from 70% to 90% of V_T. Hence, V_T measurement of [^{11}C]SL25.1^{1}88 PET is an excellent estimation of MAO-B concentration.

INTRODUCTION

Monoamine oxidase B (MAO-B) is an important enzyme on the outer mitochondrial membrane found mainly in serotonin releasing neurons and astrocytes in the brain.[1–3] It has several key roles including metabolizing monoamines such as dopamine, norepinephrine, benzylamine, and tyramine, but also influencing apoptosis and oxidative stress.[1]

Given these roles it has been proposed that abnormalities of MAO-B level and function contribute to the pathology of Alzheimer's disease, Parkinson's disease, Huntington's disease, major depressive disorder, and substance abuse.[1] To date, investigations have largely focused on Alzheimer's disease, for which abnormally elevated MAO-B levels in the prefrontal cortex are frequently found,[4] and Huntington's disease, for which elevated MAO-B level in the striatum was reported,[5] and cigarette smoking, for which globally reduced MAO-B binding was found.[6] Selective MAO-B inhibitor therapeutics have been approved for the treatment of major depressive disorder and Parkinson's disease and are under development for Alzheimer's disease. The broad range of illness for which abnormal MAO-B levels are implicated suggest high impact on diseases for society. Investigations of MAO-B in this broader range of conditions could be facilitated by the availability of highly quantitative MAO-B imaging methods with positron emission tomography (PET).

Several MAO-B radiotracers for PET have been developed but only [^{11}C]L-deprenyl[7] and its derived [^{11}C]L-deprenyl-D2[8] have

been evaluated in vivo in humans. These radioligands are irreversible and selective for MAO-B. However, they have metabolites (R(−) methamphetamine and R(−) amphetamine)[9,10] that are brain penetrant, bind specifically to monoamine transporters, which may influence the time-activity curves (TACs) from which parameters related to MAO-B activity are derived. [^{11}C]L-deprenyl-D2 represents an improvement on [^{11}C]L-deprenyl as it reduces the rate of trapping of radioligand improving the sensitivity to changes in MAO-B activity.[11] It would be even more advantageous to create a radiotracer selective for MAO-B that is both highly reversible and does not have brain penetrant metabolites.

[^{11}C]SL2511.88 is a new radiotracer that is selective for MAO-B.[12,13] On tail-vein administration in rats, < 3% radioactive metabolites are present in rat brain 30 minutes after injection (this work). In baboon, this radiotracer shows desirable properties with high brain uptake, reversible TACs, and binding values proportional to known MAO-B density.[13] Further investigations of this technique had largely stopped due to the challenges with the original radiosynthesis that required the use of carbon-11 labeled phosgene, which requires specialized apparatus, expertise and is limited to very few laboratories worldwide. To address this barrier, our group developed a synthesis route that that takes advantage of a new technology, [^{11}C]carbon dioxide fixation[14] does not require phosgene.[15]

In the present study, we sought to investigate [^{11}C]SL2511.88 as a suitable radioligand to image MAO-B in humans. We

[1]Research Imaging Centre, Centre for Addiction and Mental Health (CAMH), Toronto, Ontario, Canada; [2]Department of Psychiatry, University of Toronto, Toronto, Ontario, Canada and [3]Division of Nuclear Medicine and Molecular Imaging, Massachusetts General Hospital, and Department of Radiology, Harvard Medical School, Boston, Massachusetts, USA. Correspondence: Dr PM Rusjan, CAMH, PET Centre, 250 College Street, Toronto, Ontario, Canada M5T 1R8.
E-mail: pablo.rusjan@camhpet.ca

investigated: (1) whether one-tissue compartment or two-tissue compartment models (1-TCM of 2-TCM) fit better the TAC, (2) the identifiability of total distribution volume (V_T), the distribution volume of the specifically bound radiotracer (V_S), and the binding potential (BP_{ND}), (3) whether the regional values of such parameters were correlated with the known densities of MAO-B in the same regions; (4) the stability of these parameters in relation to the length of PET scanning; and (5) the reproducibility of these parameters under test–retest conditions.

MATERIALS AND METHODS

Radiosynthesis of [^{11}C]SL2511.88

The radiotracer was synthesized using [^{11}C]CO_2 fixation techniques as previously described.[15] Cyclotron-produced [^{11}C]CO_2 in N_2 was bubbled at 10 mL/min into a solution of (S)-1-methoxy-3-[6-(4,4,4-trifluorobutoxy)benzo[d]isoxazol-3-ylamino]propan-2-ol (0.3 μmol) and 2-tert-butylimino-2-diethylamino-1,3-dimethyl-perhydro-1,3,2-diazaphorine (BEMP; 1%, v/v) in dry CH_3CN (100 μL) in a septum-sealed 1-mL conical glass vial at ambient temperature. After 1 minute, a solution of phosphorus oxychloride (POCl$_3$) (0.2%, v/v) in dry CH_3CN (100 μL) was added. After 30 seconds, the reaction was quenched with buffer and purified by high-performance liquid chromatography before formulation and sterilization.

Metabolite Studies in Rat

All animal experiments were performed under humane conditions, with approval from the Animal Care Committee at the CAMH, and in accordance with the guidelines set forth by the Canadian Council on Animal Care. Determination of the extent of formation of radioactive metabolites in rat brain extracts and rat plasma was performed as previously described.[16] Briefly, rats (male, Sprague-Dawley, 300 to 350 g) were injected with 50 to 100 MBq of high specific activity [^{11}C]SL25.1188 (1 to 2 nmol) in 0.3 mL of buffered saline *via* the tail vein, vasodilated in a warm water bath. Rats were killed at 30 minutes after injection by decapitation, blood collected from the trunk in a heparinized tube, and the whole brain surgically removed from the skull. Brains were homogenized in 80% aq. ethanol and centrifuged. High-performance liquid chromatography radiometric analysis of plasma and brain extracts was then performed. Greater than 97% of radioactivity in brain extracts was associated with parent [^{11}C]SL25.1188 whereas in plasma it was only 40%.

Human Subjects

Seven healthy volunteers (4 men and 3 women; age, 19 to 49 years) participated in this study. All subjects were free of current medical and psychiatric illness based on history (including structured clinical interview for DSM-IV), physical examination, electrocardiogram, urinalysis (including drug screening), and blood tests (complete blood count and serum chemistry). All subjects provided written informed consent after all procedures were fully explained. Research Ethics Board approval was obtained at the Centre for Addiction and Mental Health.

Positron Emission Tomography Protocol

Each subject was scanned twice (5 ± 1 weeks of separation). The injected mass and injected radioactivity of [^{11}C]SL25.1188 ranged from 0.6 to 2.3 μg and from 7.2 to 10.5 mCi, respectively. A custom-fitted thermoplastic mask was made for each subject and used with a head fixation system during PET measurements to minimize head movement. The PET scanning was performed using a 3D High Resolution Research Tomograph (HRRT) (CPS/Siemens, Knoxville, TN, USA), which measures radioactivity in 207 slices with an interslice distance of 1.22 mm. The detectors of the HRRT are an LSO/LYSO phoswich detector, with each crystal element measuring $2 \times 2 \times 10$ mm^3. A transmission scan, measured using a single photon point source, ^{137}Cs ($t_{1/2} = 30.2$ years, E$\gamma = 662$ keV) was acquired immediately before the acquisition of the emission scan. This transmission scan was subsequently used to correct the emission data for the attenuation of the emission photons through the head and support. After the transmission scan, [^{11}C]SL2511.88 was infused intravenously over a 30-second period at a constant rate using a Harvard infusion pump (Harvard Apparatus, Holliston, MA, USA). Data were acquired in list mode for 90 minutes after the injection of [^{11}C]SL2511.88. The emission list mode data were rebinned into a series of 3D sinograms. The 3D sinograms were gap-filled, scatter corrected and fourier rebinned into 2D sinograms The

images were reconstructed from the 2D sinograms using a 2D filtered-back projection algorithm, with an HANN filter at Nyquist cutoff frequency. The reconstructed image had $256 \times 256 \times 207$ cubic voxels measuring $1.22 \times 1.22 \times 1.22$ mm^3. In addition, for frame realignment purposes each image was reconstructed without attenuation correction using three iterations of iterative reconstruction.[17,18]

The images were reconstructed into 28 time frames: The first frame was of variable length being dependent on the time between the start of acquisition and the arrival of [^{11}C]SL2511.88 in the tomograph field of view. The subsequent frames were defined as 5×30 seconds, 1×45 seconds, 2×60 seconds, 1×90 seconds, 1×120 seconds, 1×210 seconds, and 16×300 seconds. All images were decay corrected.

Head movement in the dynamic PET acquisition was corrected using frame-by-frame realignment. Low noise, nonattenuation-corrected images (created with iterative reconstruction) were used to optimize the frame-by-frame realignment process. A normalized mutual information algorithm was applied with SPM8 (Wellcome Trust Centre for Neuroimaging, London, UK) to coregister each frame to the frame from 12.25 to 17.25 minutes after the radioligand arrives to the field of view (frame number 13), which showed a high signal-to-noise ratio. Parameters from the normalized mutual information were applied to the corresponding attenuation-corrected dynamic images to generate a movement-corrected dynamic image.

Measurement of [^{11}C]SL2511.88 in Plasma

Arterial sampling was withdrawn continuously for the first 22 minutes from the radial artery cannula and counted using an automatic blood sampling system (ABSS, Model # PBS-101 from Veenstra Instruments, Joure, Netherlands). Polytetrafluoroethylene tubing was used to minimize tube adhesion of [^{11}C]SL2511.88. The rate of the blood pump was 350 mL/h the first 7.25 minutes and then slowed to 150 mL/h. In addition, manual samples were taken close to the wrist of the subject at $t = 3.5, 7, 12, 15, 20, 30, 45, 60,$ and 80 minutes at volumes between 5 and 10 mL. After the manual samples were taken at 12, 15, and 20 minutes, the ABSS line was rinsed with a saline solution.[19] Hematocrit (HCT) was measured from a sample acquired before the radioligand injection. Free fraction in plasma was determined by the ultrafiltration method.[20]

An aliquot of each manual blood sample was taken to measure radioactivity concentration in total blood. Samples at $t = 7, 12, 15,$ and 20 minutes were used to calibrate the ABSS. The remaining blood was centrifuged (1,500 g, 5 minutes) and a plasma aliquot counted together with the total blood sample using a Packard Cobra II gamma counter (Perkin-Elmer, Waltham, MA, USA) cross-calibrated with the PET system. The blood-to-plasma ratios ($[wb]/[p](t)$) were determined from the manual samples to generate the plasma TAC derived from the blood TAC measured by the ABSS and extended with the manual samples from 22 minutes to 80 minutes. A mono-exponential function

$$\frac{[wb]}{[p]}(t) = (1 - HCT) + y_0 + a(1 - \exp(-bt)) \tag{1}$$

with $y_0 > 0$, $b > 0$

was used to fit the blood-to-plasma ratios with HCT fixed to the measured value. The remaining volume of each manual plasma sample was used to determine the fraction of parent radioligand in plasma ($P(t)$) by reverse-phase radiochromatogram.[21] $P(t)$ was fitted with a Hill type function:

$$P(t) = \left(1 - \frac{at^b}{c^b + t^b}\right) \tag{2}$$

For the kinetic analysis, the input function was a metabolite-corrected plasma curve generated by multiplying the plasma TAC by the fraction of parent radiotracer. The input function and the blood TAC were extended from 80 to 90 minutes using an exponential extrapolation from the discrete samples at 30, 45, 60, and 80 minutes of parent compound in plasma and blood, respectively.

Magnetic Resonance Image and Regions of Interest Delineation

For the anatomic delineation of regions of interest (ROIs), a brain magnetic resonance image was acquired for each subject. The magnetic resonance scans were performed on a Discovery MR750 3.0T GE scanner (Milwaukee, WI, USA) equipped with an 8-channel headcoil. 2D axial proton density images were acquired as follows: fast spin echo imaging, echo time/repetition time/echo train length = MinFull/6s/8, receiver BW ± 15.63 kHz, field of view = 22 cm, 256×256 sampling matrix, slice thickness = 2 mm and a parallel imaging acceleration factor of 2. Regions of interest for the

cerebellar cortex, head of the caudate (hereafter referred to as caudate), putamen, frontal cortex, temporal cortex, anterior cingulate cortex, thalamus, and pons were automatically generated based on individual proton density-magnetic resonance images using in-house imaging pipeline, ROMI.[22] ROMI utilizes computer vision techniques based on the probabilities of gray matter to fit a standard template of ROIs to an individual high-resolution magnetic resonance image scan. The individual MRIs are then registered to a frame averaged PET image so that the individual refined ROI template is transformed to the PET image space to allow the TAC generation from each ROI. Coregistration was done using SPM2 (Wellcome Trust Centre for Neuroimaging, London, UK), which optimizes a measure of normalized mutual information.[23] Activities measured were normalized to standard uptake value (SUV) dividing by injected dose/weight of the subject.

Kinetic Analysis

Following the definitions proposed in a consensus nomenclature for reversibly binding radioligands,[24] TAC data were analyzed with 1-TCM to estimate K_1^{1TCM} and k_2^{1TCM} and V_T^{1TCM}, 2-TCM to estimate K_1, k_2, k_3, k_4, V_T, V_S, and BP_{ND} and Logan graphical analysis to estimate V_T^{LG}.[25,26] Postmortem findings have previously shown that MAO-B is widely distributed throughout the brain, hence a reference region method for the kinetic analysis was not studied.

V_T is equal to the ratio at equilibrium of the concentration of radioligand in tissue to that in plasma. V_T includes the concentrations of all radioligand in tissue (i.e., specific binding and nondisplaceable uptake (nonspecifically bound and free radioligand in tissue)). The value of V_T can be estimated from the rate constants, for 1-TCM as $V_T^{1TCM} = \frac{K_1^{1TCM}}{k_2^{1TCM}}$ and for 2-TCM as $V_T = \frac{K_1}{k_2}\left(1 + \frac{k_3}{k_4}\right)$. In addition, for the 2-TCM it is possible to estimate directly the distribution volume of the specific compartment V_S (i.e., the ratio at equilibrium of the specifically bound radioligand to that of total parent radioligand in plasma) as $V_S = \frac{K_1}{k_2}\frac{k_3}{k_4}$ and $BP_{ND} = k_3/k_4$ (i.e., a ratio at equilibrium of specifically bound radioligand to that of nondisplaceable radioligand in tissue[27]).

Delay and Dispersion

The radioactivity in the blood, as measured by the ABSS, $C_m(t)$, was corrected for delay and dispersion using: $C_m(t) = d(t) \otimes C_b(t-\delta)$ where $C_b(t)$ is the radioactivity in blood, $d(t)$ is the dispersion, δ is the delay, and $\otimes$ is the convolution operator. The dispersion was modeled by a mono-exponential function [28,29]: $d(t) = \frac{1}{\tau}e^{-t/\tau}$ where τ is the dispersion constant. The dispersion constant τ was 10 seconds. This value was measured experimentally with the pump rate at 350 mL/h.

The deconvolution was performed iteratively using the Landweber method (30 iterations in the Fourier space) (Equation (44) in ref 30, referred as 'reblurred' Van Cittert): $\hat{C}_b^{(k)}(\omega) = \hat{C}_b^{(k-1)}(\omega) + 0.5\,\overline{\hat{d}}(\omega)\left[\hat{C}_m(\omega) - \hat{d}(\omega)\hat{C}_b^{(k-1)}(\omega)\right]$, where $\hat{C}_b^{(k)}(\omega)$ is the fast Fourier transform of $C_b(t)$ at iteration k, $\hat{d}(\omega) = \frac{1}{\tau}\left(\frac{1}{\tau} + j\omega\right)^{-1}$ is the Fourier transform of $d(t)$ and $\hat{C}_b^{(0)}(\omega) = 1$ for each frequency ω. Setting properly the number of iterations, this algorithm produces a dispersion-corrected function with low noise. In a noise-free context, a very high number of iterations would be wished, however in a real case, too many iterations would increase the noise in the output. On the other extreme, a low number of iterations would lose some high frequency components producing an undesirable smoothed output (see Supplementary Material for more information).

For the estimation of δ, the initial rise of the TACs was approximated by the whole brain TAC 'head curve' $H_c(t)$, derived from the tomograph prompts coincidence rate minus the random coincidence rate. $H_c(t)$ has the advantage over the regional TACs that it can be calculated on a second-by-second basis being practically noise free. δ was estimated by fitting the rise of the $H_c(t)$ to its peak to a 1-TCM with $C_b(t)$ as an input function:

$$H_c(t) = K_1 e^{-k_2 t} \otimes C_b(t-\delta) \tag{3}$$

δ was fixed to the same value for all ROIs.

Nonlinear Least Square Fitting

Nonlinear fitting of the kinetic models was performed with the Levenberg-Marquardt algorithm using a trust-region implemented in the function lsqcurvefit() from the MATLAB optimization toolbox (v5.1) (Mathworks, Natick, MA, USA). The independent variables were the rate constants.

Each model configuration was implemented to account for the contribution of activity from the cerebral blood volume assuming that cerebral blood volume was 4% of the cortical gray-matter tissue.[31]

The percent coefficient of variation (COV = 100% standard error/mean) was used to measure the identifiability of the kinetic variables. The standard error was estimated from the diagonal of the covariance matrix. A smaller COV indicates better identifiability.

All data points were included in the fitting and brain data for each frame were weighted relative to other frames based on the trues T_i in the field of view during the frame i in the following way[32]:

$$w_i = \frac{\left(t_i^e - t_i^s\right)^2}{d_c^2 T_i} \tag{4}$$

where t_i^s and t_i^e are the frame start and end time and d_c the decay correction factor: $d_c = \lambda_c\left(t_i^e - t_i^s\right)/\left(e^{-\lambda_c t_i^s} - e^{-\lambda_c t_i^e}\right)$ with $\lambda_C = 3.4 \times 10^{-2}$ per minute, that is, the decay constant of ^{11}C.

Statistics

Goodness of fit was evaluated using the Akaike Information Criterion (AIC)[33] and the Model Selection Criterion (MSC).[34] Lower AIC and higher MSC values were indicative of a better fit. Group data are expressed as mean ± SD.

The test–retest reproducibility was evaluated in three ways: (1) within-subject variability and between-subject variability were calculated and expressed as a standard deviation and COV, (2) test–retest variability (TRV) was calculated as the mean across subjects of the ratio of the absolute difference between measurements to average of the measurements, and (3) reliability (intraclass correlation coefficient (ICC)) calculated according to the following equation:

$$ICC = \frac{BSMSS - WSMSS}{BSMSS + WSMSS}$$

where BSMSS and WSMSS are the mean sum of squares between and within subjects, respectively. This coefficient is an indicator of the relative contributions of the two sources of variance and while a value of -1 is associated with all variability attributable to within-subject variance, a value of 1 is associated with all variability associated with between-subject variance.

RESULTS

Arterial Blood Analysis

Radioactivity in blood (Figure 1) reaches a maximum of 6.8 SUV at 70 seconds after injection, followed by a quick washout. The ratio of blood to plasma started in a value close to 1-HCT (hematocrit) and after 30 minutes reached a plateau at around 0.99 (Supplementary Figure S2). The mono-exponential (Equation (1)) fitted the discrete samples with HCT = 0.42 ± 0.04, $y0 = 0.04 ± 0.05$, $a = 0.37 ± 0.10$ and $b = 0.14 ± 0.07$ 1/min. Reversed-phase high-performance liquid chromatography showed the presence of one radioactive metabolite of [11C]SL25.1188. The radiometabolite eluted earlier than the parent compound, indicating that it was more polar. The parent compound metabolism was slow and at 80 minutes it was still responsible for more than 70% radioactivity in plasma. A Hill function (Equation (2)) fitted the measured values ($r = 0.97 ± 0.04$) with $a = 0.21 ± 0.08$, $b = 2.0 ± 0.6$ and $c = 591 ± 481$ seconds (Supplementary Figure S3). The low amount of radioactivity was responsible for the variability in determining the fraction of parent compound at later times. In one scan the determination of metabolism at 80 minutes was not possible and for the other two scans the last sample was neglected during the fitting due to the large error introduced by their inclusion.

The average curve of unmetabolized [11C]SL25.1188 in plasma taken into account the correction by dispersion (Figure 1) reaches a maximum of 10 SUV 60 seconds after injection and thereafter rapidly declines. The radioactivity 2 minutes after the peak is 10% of the peak value. Free fraction was 0.82 ± 0.07% ($n = 10$).
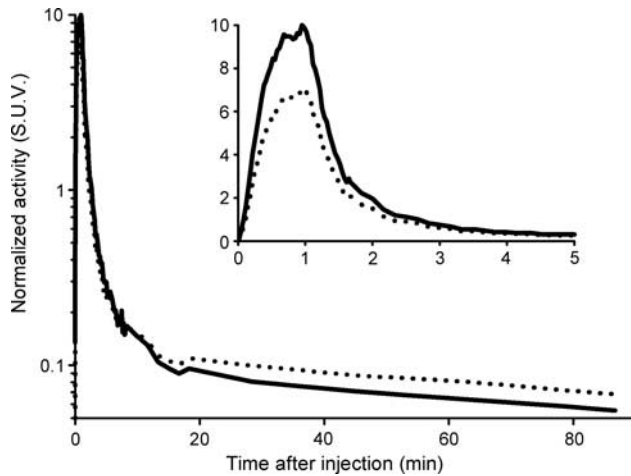
Figure 1. Average ($n = 14$) of the time course of the radioactivity due to parent compound in plasma (solid line) and the radioactivity in blood (dotted line) taken into account dispersion correction ($\tau = 10$ seconds).

Brain Uptake

After [^{11}C]SL25.1188 injection, all subjects showed high brain uptake of radioactivity that peaked between 2 and 6 minutes across the regions and declined more quickly in regions known to have lower MAO-B levels as compared with regions with higher concentrations of MAO-B (Figure 2; Supplementary Figure S1). At one extreme, the caudate showed a peak of 5.5 SUV at 6 minutes follow by a slow washout, such that at the end of the scan the activity was reduced only by 15% respect to the peak value. On the other, the cerebellar cortex showed a peak of 4.7 SUV earlier at 2 minutes followed by a quick washout, showing at the end of scan an activity 54% lower than the peak value. The cortical areas peaked simultaneously to the cerebellum at 5.2 SUV and then washed out to values 40% lower than of the peak value. The putamen and thalamus peaked higher and earlier than caudate, and presented a faster washout. The pons peaked lower than the rest of the ROIs. Radiotracer uptake in the PET image was consistent with the postmortem studies of MAO-B distribution.[2,35]

Kinetic Analysis

Compartmental model. We compared 1-TCM and 2-TCM by studying the results obtained from the full 90-minute session. With exception of the caudate, for each ROI of each scan the 2-TCM model provided a better fit than the 1-TCM (Figure 3) presenting a lower AIC and a higher MSC (paired *t* test $P < 10^{-5}$; Supplementary Table S1). For a single subject (test scan and retest scan) in the caudate the 1-TCM presented slightly lower AIC ($< 0.1\%$) and higher MSC ($< 0.1\%$); however, a pair *t*-test still showed 2-TCM to have an overall better fit of the TACs ($P = 0.0015$ for MSC and AIC).

Identifiability. Results obtained with the 2-TCM (averaging test and retest) are summarized in Table 1. V_T calculated with the 2-TCM from 90 minutes of scan data presented very good identifiability for all the ROIs ($2 < COV(V_T) < 8\%$). V_S presented similar identifiability ($2 < COV(V_S) < 8\%$) across ROIs with the exception of the caudate where the identifiability was slightly poorer ($COV(V_S) = 14\%$). BP_{ND} and K_1/k_2 were identifiable ($COV(BP_{ND}) < 15\%$) for big ROIs, that presented faster washout, but not for the other ROIs ($COV(BP_{ND}) > 30\%$). While K_1 (0.5 ± 0.1) was identifiable the rest of the rate constants was not identifiable independently.

Rank order. The rank order of V_T (mL/cm^3) was caudate (59 ± 10) > thalamus (55 ± 7) > putamen (52 ± 8) > anterior cingulate
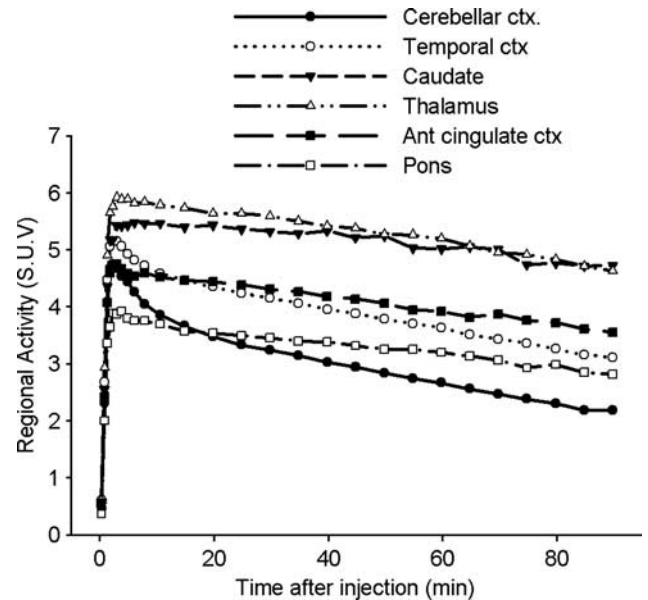

Figure 2. Average ($n = 14$) regional time-activity curve (standard uptake value, SUV) obtained after injection of [^{11}C]SL25.1188. Prefrontal cortex and putamen are omitted because they highly overlap with the temporal cortex and the thalamus, respectively.
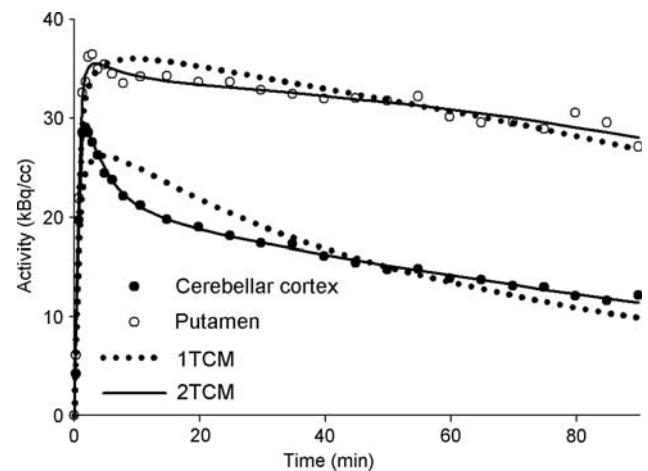

Figure 3. Regional activities in the cerebellar cortex (black circles) and putamen (white circles) for a single scan. Circles are the measured values; continues lines are the best fitting with a two-tissue compartment model (2-TCM) and the dotted lines are the best fitting with a one-tissue compartment model (1-TCM).

cortex (40 ± 6) > frontal cortex ≈ temporal cortex (33 ± 4) ≈ Pons > cerebellar cortex (22 ± 4). The rank order was preserved for V_S. On the basis of the 2-TCM estimations, V_S ranged from $80 \pm 4\%$ (cerebellum) to $90 \pm 6\%$ (ant. cingulate cortex) of V_T.

Reproducibility. Retest scan was performed 5 ± 1 weeks after the first scan (test). There was no order effect of V_T, V_S, or BP_{ND} (e.g., for V_T in Supplementary Figure S4). Table 2 shows the results of the reproducibility experiment. V_T and V_S for 90 minutes scan data showed a similar pattern and close values for the reproducibility study. While the between-subject COV of V_T ranged from 14% (prefrontal cortex) to 33% (pons), the within-subject COV was stable between 9% (cerebellar cortex) to 12% (caudate).

The TRV for V_T was between $10 \pm 7\%$ (thalamus) and $15 \pm 6\%$ (caudate). Regional ICCs for V_T ranged between 0.37 and 0.86. The

Table 1. Regional kinetic parameter (mean ± SD) of seven subjects obtained with a 2-TCM using full length of scan data (90 minutes)

	K_1 (mL/min per mL)	K_1/k_2 (mL/cm^3)	k_3 (1/min)	k_4 (1/min)	BP$_{ND}$	V_S (mL/cm^3)	V_T (mL/cm^3)
Cerebellar ctx.	0.48 ± 0.06 (2 ± 1)	4.36 ± 0.75 (11 ± 3)	0.14 ± 0.03 (15 ± 5)	0.035 ± 0.005 (8 ± 3)	4.2 ± 1.2 (13 ± 4)	18.0 ± 3.7 (4 ± 1)	22.4 ± 3.9 (3 ± 1)
Temporal ctx.	0.54 ± 0.09 (2 ± 0)	4.15 ± 0.94 (9 ± 3)	0.24 ± 0.05 (9 ± 4)	0.033 ± 0.005 (4 ± 2)	7.4 ± 2.1 (9 ± 4)	29.1 ± 4.3 (2 ± 1)	33.3 ± 4.4 (2 ± 1)
Frontal ctx.	0.53 ± 0.10 (2 ± 1)	4.33 ± 1.07 (11 ± 5)	0.25 ± 0.07 (13 ± 7)	0.036 ± 0.005 (5 ± 3)	7.2 ± 3.0 (13 ± 6)	28.7 ± 4.1 (2 ± 1)	33.0 ± 4.0 (2 ± 1)
Caudate head	0.51 ± 0.09 (6 ± 3)	10.05 ± 6.94 (63 ± 28)	0.32 ± 0.26 (73 ± 46)	0.039 ± 0.013 (31 ± 13)	9.9 ± 10.4 (74 ± 39)	49.1 ± 11.0 (14 ± 13)	59.2 ± 9.7 (7 ± 3)
Putamen	0.57 ± 0.08 (4 ± 1)	6.48 ± 2.59 (31 ± 12)	0.29 ± 0.12 (33 ± 16)	0.036 ± 0.007 (14 ± 6)	8.7 ± 5.4 (35 ± 15)	45.7 ± 8.5 (6 ± 3)	52.2 ± 7.7 (4 ± 2)
Thalamus	0.59 ± 0.05 (5 ± 2)	6.38 ± 3.86 (35 ± 14)	0.37 ± 0.24 (35 ± 16)	0.034 ± 0.007 (16 ± 7)	12.6 ± 10.7 (39 ± 15)	48.8 ± 8.2 (6 ± 4)	55.2 ± 7.0 (4 ± 2)
Anterior cingulate	0.49 ± 0.08 (5 ± 1)	3.88 ± 2.51 (32 ± 14)	0.37 ± 0.15 (31 ± 21)	0.033 ± 0.009 (13 ± 6)	12.7 ± 7.5 (35 ± 19)	36.3 ± 6.0 (6 ± 5)	40.2 ± 5.7 (4 ± 1)
Pons	0.39 ± 0.06 (5 ± 2)	4.58 ± 1.94 (35 ± 14)	0.25 ± 0.05 (38 ± 15)	0.032 ± 0.005 (17 ± 6)	8.1 ± 5.1 (39 ± 15)	28.9 ± 7.3 (7 ± 3)	33.4 ± 7.9 (6 ± 2)

2-TCM; two-tissue compartment model; BP$_{ND}$, binding potential; COV, coefficient of variation. Each subject was scanned twice. Values between parentheses indicate the identifiability (%COV) of the parameters.

Table 2. Reproducibility of [^{11}C]SL25.1188 total distribution volume (V_T), distribution volume of the specifically bound radiotracer (V_S) and binding potential (BP$_{ND}$) derived via 2-TCM

90 minutes data	V_T (mL/cm^3)					V_S (mL/cm^3)					BP$_{ND}$				
	Mean	BSSD (%CV)	WSSD (%CV)	TRV ± SD (%)	ICC	Mean	BSSD (%CV)	WSSD (%CV)	TRV ± SD (%)	ICC	Mean	BSSD (%CV)	WSSD (%CV)	TRV ± SD (%)	ICC
Cerebellar ctx.	22.4	5.3 (23)	2.0 (9)	11 ± 7	0.739	18	5.1 (28)	1.8 (10)	12 ± 10	0.771	4.2	1.3 (30)	1.1 (25)	28 ± 17	0.18
Temporal ctx.	33.3	5.4 (16)	3.4 (10)	12 ± 9	0.438	29.1	5.3 (18)	3.2 (11)	12 ± 12	0.471	7.4	2.2 (30)	2.0 (27)	28 ± 25	0.109
Prefrontal ctx.	33	4.7 (14)	3.2 (10)	11 ± 9	0.379	28.7	5.3 (19)	2.7 (9)	11 ± 10	0.6	7.2	3.5 (48)	2.5 (35)	28 ± 24	0.303
Caudate head	59.2	11.8 (20)	7.4 (12)	15 ± 6	0.442	49.1	15.1 (31)	5.4 (11)	14 ± 12	0.77	9.9	9.6 (97)	11.1 (112)	97 ± 50	−0.146
Putamen	52.2	9.5 (18)	5.8 (11)	13 ± 9	0.457	45.7	10.9 (24)	5.8 (13)	14 ± 11	0.559	8.7	6.7 (77)	3.9 (45)	38 ± 27	0.497
Thalamus	55.2	9.1 (16)	4.4 (8)	10 ± 7	0.615	48.8	11.4 (23)	3.8 (8)	9 ± 10	0.796	12.6	14.7 (116)	5.4 (42)	39 ± 20	0.765
Ant cingulate ctx.	40.2	7.0 (17)	4.3 (11)	13 ± 10	0.445	36.3	7.3 (20)	4.6 (13)	16 ± 11	0.442	12.7	10.5 (83)	3.2 (25)	31 ± 27	0.83
Pons	33.4	11.1 (33)	3.1 (9)	11 ± 9	0.856	28.9	10.3 (36)	3.0 (10)	13 ± 10	0.84	8.1	3.2 (40)	6.2 (77)	69 ± 58	−0.577

BSSD, between-subject standard deviation; CV, %standard deviation/mean; TRV, the mean across the subjects of the ratio absolute value of the difference between measurements to average of the measurements; ICC, intraclass correlation coefficient; WSSD, within-subject standard deviation.
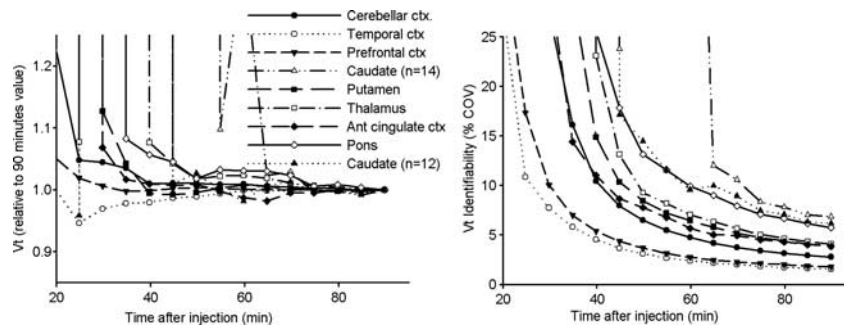

Figure 4. Regional average convergence of V_T to the final value at 90 minutes (left) and identifiability (right). For all the regions the 14 scans are considered. For the caudate, an average of 12 scans are shown as 2 time-activity curves gave solutions with low identifiability for length of scan below 70 minutes when two-tissue compartment model (2-TCM) was applied. COV, coefficient of variation.

reproducibility of BP$_{ND}$ was poor even for the ROI in which some degree of identifiability was present (between-subject COV >30%, within-subject COV >25% TRV >28%.

Stability over time. Figure 4 (Left) shows the temporal convergence of the V_T to the final value at 90 minutes for each ROI. With the exception of the caudate, at 45 minutes V_T or V_S (Supplementary Figure S5) are within 5% of the final value at 90 minutes.

The caudate had the highest uptake and therefore the TAC presented the slowest washout, and due to the small size of the ROI, TACs were noisy. In only one scan of two participants, 2-TCM provided an unacceptable solution (COV(V_T) >50%) when the length of the scan was shorter than 70 minutes. Figure 4 shows results for the caudate including and excluding these two scans. When those two scans are excluded the V_T in caudate at 45 minutes is within 5% of the final value.

COV(V_T) (Figure 4, Right) improved continuously with the length of the scan ranging from 3% to 18% at 45 minutes, to <10% at

60 minutes and <7% at 90 minutes. Reproducibility studies (Supplementary Table S2) for V_T showed that while between-subject variability for V_T was relatively constant between 45 minutes and 90 minutes, within-subject variability, TRV and ICC improved with the length of the scan.

Linear Graphical Analysis

V_T^{LG} values estimated with Logan graphical approach [25] for $t^* = 7.75$ minutes (frame #11) gave the best trade off correlation and bias respect of 2-TCM ($r^2 = 0.98 = 0.98$, V_T^{LG} underestimate 3.5% V_T^{2TCM}). Using total least squared method [26] (V_T^{TLS})[26] the correlation increases to $r^2 = 0.99$, and the underestimation decreases to 2.4%. The linear regressions were $V_T^{LG} = 0.93 \times V_T^{2TCM} + 1.2$ and $V_T^{TLS} = 0.96 \times V_T^{2TCM} + 0.6$ (Supplementary Figure S6). Test–retest results for the Logan method (Supplementary Table S3) were subtly better than for the 2-TCM.
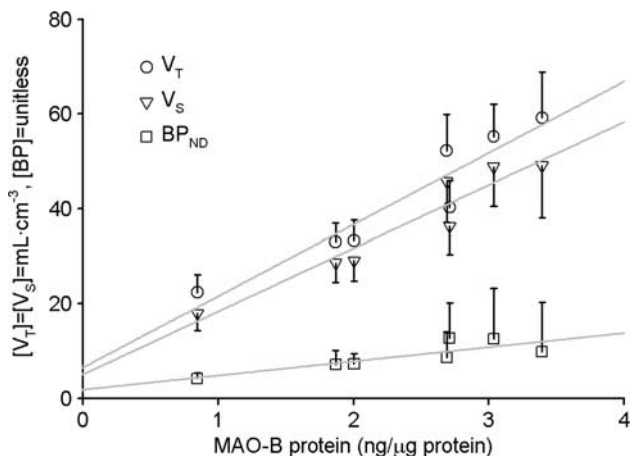
888

Figure 5. Comparison of regional average ($n = 14$) in vivo [^{11}C]SL25.1188 V_T, V_S, and BP_{ND} and in vitro concentration of monoamine oxidase B (MAO-B) determined by inmunoblotting in autopsied normal human brain ($n = 6$) published previously by Tong.[35] Regions in order of in vitro concentration are cerebellar cortex, prefrontal cortex, temporal cortex, putamen, anterior cingulate cortex, thalamus, and caudate. Vertical lines represent the SD, lines represent the best linear fit (V_T: $r^2 = 0.9$, $P = 0.001$, V_S: $r^2 = 0.92$, $P = 0.0006$ and BP_{ND}: $r^2 = 0.7$, $P = 0.02$).

Comparison with Human Postmortem Data

Our group recently published an extensive set of ROIs data showing regional postmortem concentration of MAO-B by quantitative immunoblotting in a set of healthy subjects with a wide age range.[35] Correlations (Figure 5) between the regional magnitudes to quantify [^{11}C]SL25.1188 in this work and the ones in the postmortem study are excellent: $V_T = 15.1 \times [MAOB] + 6.6$ ($r^2 = 0.9$, $P = 0.001$), $V_S = 13.3 \times [MAOB] + 5.1$ ($r^2 = 0.92$, $P = 0.0006$) and $BP_{ND} = 3.0 \times [MAOB] + 1.9$ ($r^2 = 0.7$, $P = 0.02$).

DISCUSSION

This work describes the first in vivo quantification of [^{11}C]SL25.1188 for estimation of MAO-B density in human brain. Present results indicate that [^{11}C]SL25.1188 penetrates the brain–blood barrier and shows high radiotracer uptake into brain tissue. The 2-TCM describes the TACs of [^{11}C]SL25.1188 optimally as compared with the 1-TCM. Also, the V_T provided by the 2-TCM presents an excellent identifiability (COV < 8%) and significantly correlates with the known concentration of MAO-B in brain. Test–retest study for V_T with 5 weeks separation between scans showed (averaging across ROIs): (1) a TRV of 12%, (2) between-subject COV of 20%, and (3) acceptable within-subject variability of around 10%.

This study did not include blocked experiments, therefore despite the good identifiability, reproducibility and correlation between V_S and the known concentration of MAO-B postmortem, the value for V_{ND} has not been directly measured. In the absence of blocked studies there is a risk that V_S and BP_{ND} reflect a good fit to the TACs but do not represent physiologic quantities. Therefore, until blocked experiments are performed we believe that the best magnitude to quantify MAO-B binding is V_T.

V_T is only a good parameter to quantify specific binding when the distribution volume of the free and nonspecific binding (V_{ND}) is proportionally low. If V_{ND} was the same in all the ROIs, a typical assumption in PET field, then V_{ND} could be estimated from the intercept (6.6 mL/cm^3) of the plot showing the correlation of V_T against postmortem densities of MAO-B (Figure 5). This value is not very different from the one calculated with the 2-TCM (in average 5.5 mL/cm^3). A value of $V_{ND} = 6.6$ mL/cm^3 suggests that between

70% (cerebellar cortex) and 89% (caudate) of V_T corresponds to specific binding and also supports the use of V_T as the best outcome measure to quantify [^{11}C]SL25.1188 in human brain.

The convergence of V_T to their final value is within 5% at 45 minutes after injection for most of the ROIs. However, the identifiability of the parameters and the TRV continue to improve with the length of the scan. For the caudate (small ROIs with noisy TAC and with high concentration of MAO-B) less of 70 minutes of scan in two cases gave an unacceptable identifiability. The optimal length of scan will depend on the tradeoff between size and concentration of MAO-B of the ROI of each particular study. For example, more than 60 minutes of scan data does not improve the quantification for the anterior cingulate cortex, which as delineated in this work, was a small ROI ($\sim 1,600$ voxels ≈ 2.9 cm^3) with moderate to high levels of MAO-B.

Logan graphical method V_T^{LG} correlates well with V_T^{2TCM} therefore could be a good option for parametric maps of V_T provided noise induced bias can be managed (e.g., producing the map in the wavelet space[36]) Test–retest results for the Logan method were subtly better than the 2-TCM.

The ratio of whole blood to plasma was extrapolated from the first data sample at 3.5 minutes to the time of injection using a mono-exponential (Equation (1)). As this ratio was only 7% higher than 1-HCT it is apparent that the radiotracer partitions almost exclusively into the plasma or penetrates into red blood cells only slowly. The result was confirmed in an in vitro experiment: blood samples were incubated with radiotracer at 37°C, centrifuged, and both phases counted for radioactivity. The distribution ratio of radioactivity in plasma to red cells was greater than 5 after both 30 seconds and 20 minutes of incubation.

The constant of dispersion $\tau = 10$ seconds measured for [^{11}C]SL25.1188 with the rate pump at 350 mL/h in saline solution is higher than for other radiotracers [^{18}F]fluoride ($\tau \sim 3.5$ seconds) or [^{11}C]FLB ($\tau \sim 5$ seconds). We attribute that to some degree of stickiness from the radioligand to the tube of the ABSS. It has been reported[19] that stickiness to the ABSS tubing has been related to residual radioactivity during the flushing periods. We indeed observed in some cases a low residual radioactivity in the ABSS during the flushing periods. However, the residual was too low (around 1 count per second in the 1,022 keV window) for precise quantification and the amount depended strongly on the length of the flushing period. For example, in the typical experimental set-up for studying dispersion on ABSS,[37] using the ABSS pump to flush, 1 minute of flushing with the pump at 350 mL/h (6 mL) removed the radioligand completely which would imply that the stickiness was weak or at least did not accumulate irreversibly. Finally analyzing the data ignoring dispersion or with $\tau = 5$ seconds did not show significant changes in the parameters measured when the length of scan was 60 minutes or above provided the delay was adjusted properly (Equation (3)).

Despite the fact that cerebral blood volume varies in the brain, we used the fraction volume of blood in the ROI (V_b) fixed to 4%, as when V_b was fitted as a variable, it did not show identifiability.

The ED_{50} of the radiotracer for occupancy of MAO-B has not been established in human subjects. The issue whether the radioligand was injected at tracer dose has not been addressed in this study. A plot between mass injected and V_T shows no observable effect of the mass on tracer binding in regions of both high and low MAO-B concentrations (Supplementary Figure S6).

The average value of K_1 (0.51 mL/min per mL) is similar to that measured in anesthetized baboons for this radiotracer and it is consistent with the lipophilicity of the radioligand. It can be predicted with the in silico model of Guo et al[38] ($K_1 = 0.52$ mL/min per mL) using an in silico estimation for cLogD = 3.137 and a McGowan Volume Vx = 236.81 cm^3/mol. The experimental value for Log D was 3.34 ± 0.05 ($n = 8$).

The value of K_1 is close to the typical healthy human blood flow suggesting a high first past extraction fraction, which is remarkable

taking into account the low plasma-free fraction measured ($0.82 \pm 0.07\%$ ($n = 10$)). It would suggest that the kinetics of protein binding (specifically the off rate) may be fast compared with the transit time of the radiotracer in a brain capillary.[39]

CONCLUSION

[11C]SL25.1188 shows high penetration into human brain and good reversibility properties. V_T of [11C]SL25.1188 can be reliably quantified with 2-TCM, and either 45 or 90 minutes data acquisition is needed depending on the ROI. V_T of [11C]SL25.1188 shows good reproducibility (TRV $\approx 12\%$) and is an excellent predictor of the known concentration of MAO-B postmortem in human.

DISCLOSURE/CONFLICT OF INTEREST

The authors declare no conflict of interest.

REFERENCES

1 Youdim MB, Edmondson D, Tipton KF. The therapeutic potential of monoamine oxidase inhibitors. Nat Rev Neurosci 2006; 7: 295–309.

2 Saura J, Bleuel Z, Ulrich J, Mendelowitsch A, Chen K, Shih JC et al. Molecular neuroanatomy of human monoamine oxidases A and B revealed by quantitative enzyme radioautography and in situ hybridization histochemistry. Neuroscience 1996; 70: 755–774.

3 Saura J, Kettler R, Da Prada M, Richards JG. Quantitative enzyme radioautography with 3H-Ro 41-1049 and 3H-Ro 19-6327 in vitro: localization and abundance of MAO-A and MAO-B in rat CNS, peripheral organs, and human brain. J Neurosci 1992; 12: 1977–1999.

4 Jossan SS, Gillberg PG, Gottfries CG, Karlsson I, Oreland L. Monoamine oxidase B in brains from patients with Alzheimer's disease: a biochemical and auto-radiographical study. Neuroscience 1991; 45: 1–12.

5 Mann JJ, Kaplan RD, Bird ED. Elevated postmortem monoamine oxidase B activity in the caudate nucleus in Huntington's disease compared to schizophrenics and controls. J Neural Transm 1986; 65: 277–283.

6 Fowler JS, Volkow ND, Wang GJ, Pappas N, Logan J, MacGregor R et al. Inhibition of monoamine oxidase B in the brains of smokers. Nature 1996; 379: 733–736.

7 Fowler JS, MacGregor RR, Wolf AP, Arnett CD, Dewey SL, Schlyer D et al. Mapping human brain monoamine oxidase A and B with 11C-labeled suicide inactivators and PET. Science 1987; 235: 481–485.

8 Fowler JS, Wolf AP, MacGregor RR, Dewey SL, Logan J, Schlyer DJ et al. Mechanistic positron emission tomography studies: demonstration of a deuterium isotope effect in the monoamine oxidase-catalyzed binding of [11C]L-deprenyl in living baboon brain. J Neurochem 1988; 51: 1524–1534.

9 Azzaro AJ, Ziemniak J, Kemper E, Campbell BJ, VanDenBerg C. Pharmacokinetics and absolute bioavailability of selegiline following treatment of healthy subjects with the selegiline transdermal system (6 mg/24 h): a comparison with oral sele-giline capsules. J Clin Pharmacol 2007; 47: 1256–1267.

10 Fowler JS, Volkow ND, Logan J, Schlyer DJ, MacGregor RR, Wang GJ et al. Monoamine oxidase B (MAO B) inhibitor therapy in Parkinson's disease: the degree and reversibility of human brain MAO B inhibition by Ro 19 6327. Neurology 1993; 43: 1984–1992.

11 Logan J, Fowler JS, Volkow ND, Wang GJ, MacGregor RR, Shea C. Reproducibility of repeated measures of deuterium substituted [11C]L-deprenyl ([11C]L-deprenyl-D2) binding in the human brain. Nucl Med Biol 2000; 27: 43–49.

12 Bramoullé Y, Puech F, Saba W, Valette H, Bottlaender M, George P et al. Radio-synthesis of (S)-5-methoxymethyl-3-[6-(4,4,4-trifluorobutoxy)benzo[d]isoxazol-3-yl] oxazolidin-2-[11C]one ([11C]SL25.1188), a novel radioligand for imaging monoamine oxidase-B with PET. J Labelled Comp Radiopharm 2008; 51: 153–158.

13 Saba W, Valette H, Peyronneau MA, Bramoulle Y, Coulon C, Curet O et al. [(11)C]SL25.1188, a new reversible radioligand to study the monoamine oxidase type B with PET: preclinical characterisation in nonhuman primate. Synapse 2010; 64: 61–69.

14 Rotstein BH, Liang SH, Holland JP, Collier TL, Hooker JM, Wilson AA et al. 11CO2 fixation: a renaissance in PET radiochemistry. Chem Commun 2013; 49: 5621–5629.

15 Vasdev N, Sadovski O, Garcia A, Dollé F, Meyer JH, Houle S et al. Radiosynthesis of [11C]SL25.1188 via [11C]CO2 fixation for imaging monoamine oxidase B. J Labelled Comp Radiopharm 2011; 54: 678–680.

16 Wilson AA, Garcia A, Parkes J, McCormick P, Stephenson KA, Houle S et al. Radiosynthesis and initial evaluation of [18F]-FEPPA for PET imaging of peripheral benzodiazepine receptors. Nucl Med Biol 2008; 35: 305–314.

17 Hong IK, Chung ST, Kim HK, Kim YB, Son YD, Cho ZH. Ultra fast symmetry and SIMD-based projection-backprojection (SSP) algorithm for 3-D PET image recon-struction. IEEE Trans Med Imaging 2007; 26: 789–803.

18 Comtat C, Bataille F, Michel C, Jones JP, Sibomana M, Janeiro L et al. OSEM-3D reconstruction strategies for the ECAT HRRT. IEEE Nucl Sci Symp Conf Rec 2004; 6: 3492–3496.

19 Lammertsma AA, Bench CJ, Price GW, Cremer JE, Luthra SK, Turton D et al. Mea-surement of cerebral monoamine oxidase B activity using L-[11C]deprenyl and dynamic positron emission tomography. J Cereb Blood Flow Metab 1991; 11: 545–556.

20 Gandelman MS, Baldwin RM, Zoghbi SS, Zea-Ponce Y, Innis RB. Evaluation of ultrafiltration for the free-fraction determination of single photon emission computed tomography (SPECT) radiotracers: beta-CIT, IBF, and iomazenil. J Pharm Sci 1994; 83: 1014–1019.

21 Hilton J, Yokoi F, Dannals RF, Ravert HT, Szabo Z, Wong DF. Column-switching HPLC for the analysis of plasma in PET imaging studies. Nucl Med Biol 2000; 27: 627–630.

22 Rusjan P, Mamo D, Ginovart N, Hussey D, Vitcu I, Yasuno F et al. An automated method for the extraction of regional data from PET images. Psychiatry Res 2006; 147: 79–89.

23 Studholme C, Hill DLG, Hawkes DJ. An overlap invariant entropy measure of 3D medical image alignment. Pattern Recogn 1999; 32: 71–86.

24 Innis RB, Carson R. Consensus nomenclature: its time has come. Eur J Nucl Med Mol Imaging 2007; 34: 1239.

25 Logan J, Fowler JS, Volkow ND, Wolf AP, Dewey SL, Schlyer DJ et al. Graphical analysis of reversible radioligand binding from time-activity measurements applied to [N-11C-methyl]-(−)-cocaine PET studies in human subjects. J Cereb Blood Flow Metab 1990; 10: 740–747.

26 Varga J, Szabo Z. Modified regression model for the Logan plot. J Cereb Blood Flow Metab 2002; 22: 240–244.

27 Mintun MA, Raichle ME, Kilbourn MR, Wooten GF, Welch MJ. A quantitative model for the in vivo assessment of drug binding sites with positron emission tomo-graphy. Ann Neurol 1984; 15: 217–227.

28 Iida H, Kanno I, Miura S, Murakami M, Takahashi K, Uemura K. Error analysis of a quantitative cerebral blood flow measurement using H$_2$^{15}O autoradiography and positron emission tomography, with respect to the dispersion of the input function. J Cereb Blood Flow Metab 1986; 6: 536–545.

29 Kanno I, Lammertsma AA, Heather JD, Gibbs JM, Rhodes CG, Clark JC et al. Measure-ment of cerebral blood flow using bolus inhalation of C15O2 and positron emission tomography: description of the method and its comparison with the C15O2 continuous inhalation method. J Cereb Blood Flow Metab 1984; 4: 224–234.

30 Carasso A. Linear and nonlinear image deblurring: a documented study. SIAM J Numer Anal 1999; 36: 1659–1689.

31 Ito H, Kanno I, Kato C, Sasaki T, Ishii K, Ouchi Y et al. Database of normal human cerebral blood flow, cerebral blood volume, cerebral oxygen extraction fraction and cerebral metabolic rate of oxygen measured by positron emission tomo-graphy with ^{15}O-labelled carbon dioxide or water, carbon monoxide and oxygen: a multicentre study in Japan. Eur J Nucl Med Mol Imaging 2004; 31: 635–643.

32 Lammertsma AA. Compartmental modeling in emission tomography. In: Handbook of Particle Detection and Imaging. Springer: Berlin Heidelberg, 2012, pp 1065–1081.

33 Akaike H. A new look at the statistical model identification. IEEE Trans Automat Contr 1974; 19: 716–723.

34 MicroMath. MicroMath Scientist Handbook Rev. 7EEF. Micromath: Salt Lake City, 1995.

35 Tong J, Meyer JH, Furukawa Y, Boileau I, Chang LJ, Wilson AA et al. Distribution of monoamine oxidase proteins in human brain: implications for brain imaging studies. J Cereb Blood Flow Metab 33: 863–871.

36 Rusjan P, Meyer J, Bloomfield P, Houle S. Parametric modeling of [11C]harmine acquired on the HRRT PET. J Nucl Med 2009; 50: 1417.

37 Boellaard R, van Lingen A, van Balen SC, Hoving BG, Lammertsma AA. Char-acteristics of a new fully programmable blood sampling device for monitoring blood radioactivity during PET. Eur J Nucl Med 2001; 28: 81–89.

38 Guo Q, Brady M, Gunn RN. A biomathematical modeling approach to central nervous system radioligand discovery and development. J Nucl Med 2009; 50: 1715–1723.

39 Farde L, Eriksson L, Blomquist G, Halldin C. Kinetic analysis of central [11C]raclopride binding to D2-dopamine receptors studied by PET--a comparison to the equilibrium analysis. J Cereb Blood Flow Metab 1989; 9: 696–708.